Journal of the Physical Society of Japan **94**, 074709 (2025)

Full Papers

https://doi.org/10.7566/JPSJ.94.074709

Electronic Structures of Yb_3Si_5 and Yb_3Ge_5 Studied by X-ray Absorption Spectroscopy, Resonant X-ray Emission Spectroscopy, Photoelectron Spectroscopy, and LDA+DMFT Calculations

Hitoshi Yamaoka[1,2*], Patrik Thunström[3†], Naohito Tsujii[4], Masashi Arita[5],
Eike F. Schwier[5‡], Kenya Shimada[5], Hirofumi Ishii[6], and Nozomu Hiraoka[6]

[1]*RIKEN SPring-8 Center, Sayo, Hyogo 679-5148, Japan*
[2]*Institute for R&D Promotion, Doshisha University, Kyoto 602-8580, Japan*
[3]*Department of Physics and Astronomy, Uppsala University, Box 256, 751 05 Uppsala, Sweden*
[4]*Research Center for Materials Nanoarchitectonics, National Institute for Materials Science, Tsukuba, Ibaraki 305-0047, Japan*
[5]*Hiroshima Synchrotron Radiation Center, Hiroshima University, Higashihiroshima, Hiroshima 739-0046, Japan*
[6]*National Synchrotron Radiation Research Center, Hsinchu 30076, Taiwan*

(Received March 5, 2025; revised April 20, 2025; accepted May 26, 2025; published online June 20, 2025)

Electronic structure of the intermediate valence systems Yb_3Si_5 and Yb_3Ge_5 were investigated by using high-resolution x-ray absorption spectroscopy, resonant x-ray emission spectroscopy, and photoelectron spectroscopy as a function of temperature. XAS and RXES measurements revealed that the Yb valence in Yb_3Si_5 decreased monotonically with decreasing temperature. In contrast, in Yb_3Ge_5, it remains nearly divalent and exhibits little temperature dependence from room temperature down to 23 K. Combined with theoretical fits to the magnetic susceptibility data, these results suggest that the Kondo temperature of Yb_3Ge_5 is significantly higher than that of Yb_3Si_5. The photoelectron spectra of both compounds directly identified the signatures of a Kondo resonance peak at low temperatures. Additionally, high-pressure experiments were conducted on Yb_3Si_5 and Yb_3Ge_5, revealing critical transition pressures toward the Yb^{3+} state at 10–12 and 8–9 GPa, respectively. The experimental valence-band spectra were further compared with the density of states calculations performed using the local density approximation plus dynamical mean-field theory (LDA+DMFT), which successfully reproduced the experimental bulk valence-band spectra.

1. Introduction

Among rare-earth compounds, Ce, Sm, Eu, and Yb systems are notable for their tendency to exhibit intermediate valence behavior.[1–3] In an intermediate valence compound, the thermal ground state consists of several nearly degenerate electronic configurations with different numbers of 4*f* electrons. These small energy differences between the multiplet states of the 4*f* electrons enable low-energy excitations of the valence electrons to couple directly to the strong Coulomb interaction within the 4*f* orbitals, significantly influencing the physical properties of these materials. Temperature dependence of the electronic structure is closely linked to a crossover from an incoherent thermal occupation of the low-energy configurations to a coherent superposition (Kondo singlet) of these states as the temperature decreases. This change in the electronic structure is strongly dependent on the Kondo temperature. Pressure is also a useful tool for investigating the electronic structure, as it allows control over the Kondo temperature.

Valence fluctuations have been associated with a large Seebeck coefficient, making these materials promising candidates for future thermoelectric applications.[4–6] They also show potential for other technological applications, such as electronic devices with low Schottky barriers.[7,8] Electronic structure may play a crucial role in achieving high thermoelectric performance.[9] Binary rare-earth silicides and germanides, such as Yb_3Si_5 and Yb_3Ge_5, are typical examples of materials that exhibit valence fluctuations along with excellent thermoelectric properties.[4,5,9–12]

The magnetic and transport properties of Yb_3Si_5 and Yb_3Ge_5 have been investigated in a series of studies. The magnetic susceptibility of Yb_3Si_5 exhibited signatures of valence fluctuations and was fitted using the interconfiguration fluctuation (ICF) model.[13,14] The spin fluctuation temperature was estimated to be approximately 150 K. The ICF model fitting revealed a surprisingly large variation in Yb valence with temperature, ranging from 2.3 at low temperatures to 2.8 at 800 K in Yb_3Si_5. Additionally, resistivity measurements showed Fermi liquid behavior below 50 K. For Yb_3Ge_5, the magnetic susceptibility exhibited weak temperature dependence for $T > 20$ K but increased rapidly below $T < 20$ K.[15] This behavior was also analyzed using the ICF model, yielding a spin fluctuation temperature of approximately 770 K and a relatively large valence change with temperature, from 2.1 at 4.2 K to 2.5 at 800 K. The large variation in Yb valence, as analyzed by the ICF model, motivated us to directly measure the precise Yb valence using state-of-the-art spectroscopic techniques in this study. Furthermore, the pressure dependence of the resistivity for single-crystalline Yb_3Si_5 was measured up to 60 GPa.[16] The characteristic temperature, at which the temperature derivative of the resistance reaches a maximum, exhibited a minimum of around 21 GPa.

The electronic structure of Yb_3Si_5 has been investigated using photoelectron spectroscopy (PES) over an energy range of 80 to 1253 eV by Abbati et al.[17–21] They decomposed the Yb^{2+} component of the $h\nu = 80$ eV valence band spectrum into surface, subsurface, and bulk contributions, where $h\nu$ denotes the incident photon energy. Their analysis yielded a bulk Yb valence of 2.52 at room temperature,[21] which exhibited a weak monotonic decrease to 2.44 as the temperature was lowered to 100 K.[18] In a separate analysis, Abbati et al.[17] focused on the escape depth of the emitted electrons, estimating a valence of approximately 2.6. More recently, Kuga et al.[9] performed soft x-ray and hard x-ray PES on Yb_3Si_5 at 600 and 5700 eV, respectively, and reported a Yb valence of 2.67 at 20 K.

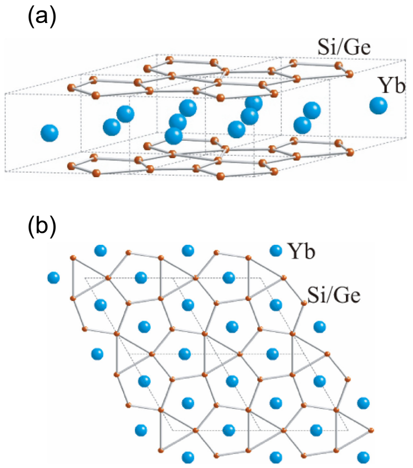

Fig. 1. (Color online) Schematic image of the Th_3Pd_5-type crystal structure of Yb_3Si_5 and Yb_3Ge_5: (a) a perspective view of *ac* plane, (b) a projection on *ab* plane.

Yb_3Si_5 and Yb_3Ge_5 crystallize in a hexagonal structure derived from the AlB_2-type arrangement.[10,14,22,23] Their structures consist of alternating Yb and Si (Ge) planes, as illustrated in Fig. 1. This layered configuration makes the samples brittle and easily cleavable. The exact atomic termination of the cleaved surface remains uncertain. However, PES analysis by Abbati et al. suggested the presence of a partially disordered monolayer of divalent Yb atoms associated with the subsurface region.[17,19] This interpretation therefore favors a strong, nearly amorphous surface reconstruction, including the outer Si layer. However, this scenario is in contrast to the observations that ordered Yb–Si layers spontaneously form when Yb was deposited on Si and annealed at temperatures as low as 600 K,[24,25] suggesting that Si layers are both thermodynamically stable and kinetically favorable to form. While this does not rule out the possibility of randomly distributed Si vacancies in the outermost Si layer — similar to the high-temperature $YbSi_{2-x}$ structure[15] — it casts doubt on the extent of surface reconstruction. Thus, a detailed high-resolution investigation of the electronic structure is necessary to clarify the nature of the subsurface layer and to accurately determine the temperature dependence of the bulk Yb valence, distinguishing between thermal occupation and Kondo screening as the dominant mechanism.

In this study, we aim to elucidate the temperature and pressure dependences of the electronic structures of Yb_3Si_5 and Yb_3Ge_5, both of which adopt the Th_3Pd_5-type crystal structure.[11,12] We investigate the temperature- and pressure-induced crossover in the electronic structures, specifically the transition from incoherent to coherent excitations. Notably, the electronic structures of Yb_3Ge_5, as well as those of Yb_3Si_5 and Yb_3Ge_5 under pressure, have not yet been fully explored. To address this, we employed resonant x-ray emission spectroscopy (RXES) and x-ray absorption spectroscopy in the partial fluorescence yield mode (PFY-XAS).[26–28] Additional insights into the electronic structure were obtained from the temperature dependence of the valence band spectra near the Fermi level (E_F), measured using ultraviolet (UV) and soft x-ray (SX) photoemission spectroscopy. Resonant PES measurements were also performed in the SX energy region. Finally, we compared our experimental results with density functional theory combined with dynamical mean-field theory (DFT+DMFT) calculations. Furthermore, high-pressure studies on Yb_3Si_5 and Yb_3Ge_5 revealed critical transitions to the Yb^{3+} state.

2. Experiments

Polycrystalline samples of Yb_3Si_5 have been prepared by melting pure Yb (99.9%) and Si (99.9999%) in an arc furnace under Ar atmosphere. Yb was enriched by 10% to compensate for the loss in the melting process. The melted ingots were annealed in evacuated quartz tubes at 973 K for 7 d. Polycrystalline samples of Yb_3Ge_5 were prepared by melting stoichiometric amounts of Yb (99.9%) and Ge (99.99%) in sealed Ta-tubes, which had been sealed by an arc under Ar atmosphere. The Ta tubes were then sealed in quartz tube under vacuum, and were heated in an electric furnace at 1443 K for 3 h and further annealed at 1273 K for 2 d. These compounds have the Th_3Pd_5-type hexagonal crystal structure (space group No. 189, $P\bar{6}2m$) with lattice constants of $a = 0.6508$ nm and $c = 0.4092$ nm for Yb_3Si_5 and $a = 0.68495$ nm and $c = 0.41765$ nm for Yb_3Ge_5, as shown in Fig. 1.[10,14,15,22] The magnetic susceptibility was measured with a superconducting quantum interference device (SQUID) magnetometer at an applied field of 1000 Oe.

PFY-XAS and RXES measurements were performed at the Taiwan beamline BL12XU, SPring-8.[26–28] The undulator beam was monochromatized by a pair of cryogenically-cooled Si(111) crystals and focused to a size of 30 (horizontal) × 40 (vertical) μm^2 at the sample position using toroidal and Kirkpatrick–Baez mirrors. A Johann-type spectrometer equipped with a spherically bent Si(620) crystal (radius of ∼1 m) was used to analyze the Yb $L\alpha_1$ ($3d_{5/2} \to 2p_{3/2}$) and Raman emissions with a solid state detector (XFlash 1001 type 1201). The overall energy resolution was estimated to be about 1 eV around the emitted photon energy of 7400 eV based on the elastic scattering. The intensities of all spectra were normalized to the incident beam intensity monitored just before the target.

Pressure dependence of the PFY-XAS spectra for Yb_3Si_5 and Yb_3Ge_5 was also measured at BL12XU, using a diamond anvil cell (DAC) with a Be gasket. Silicone oil was used as the pressure-transmitting medium. A membrane-controlled DAC was used for high-pressure experiments at room temperature. The pressure was measured based on the Raman shift of the ruby fluorescence.[29,30] Details of the experimental setup have been published elsewhere.[27,28,31]

SX and UV PES measurements were performed at the undulator beamlines BL-1 and BL-9A at the Hiroshima Synchrotron Radiation Center (HiSOR), equipped with high-resolution hemispherical electron-energy analyzers (R4000, VG-SCIENTA).[32,33] In the UV PES at BL-9A the resolution (ΔE) was approximately 10–20 meV at $h\nu = 10$–40 eV and 9 K under the vacuum pressure below 2×10^{-9} Pa, where $h\nu$ is incident photon energy. In the SX PES ΔE was approximately 40–50 meV at $h\nu = 182$ eV and 7 K under a vacuum pressure below 10^{-8} Pa. We also used light of 8.437 eV from the Xe lamp for high-resolution UV PES, where the resolution was less than 10 meV at 9 K.[34] The Fermi edge of Au evaporated on the sample holders was used to calibrate the binding energy. The energy resolution and the Fermi level were determined from fitting the Fermi edge of Au using a convolution of Gaussian and Fermi–Dirac functions. All samples were fractured in vacuum just before the measurements.

3. LDA+DMFT Calculations

A fully-charge self-consistent LDA+DMFT calculation[35,36] was performed using the full-potential linear muffin-tin orbital code RSPt[37] and the DMFT implementation described in Refs. 38–41. The strongly correlated Yb 4*f* states were treated using the Exact Diagonalization (ED) impurity solver.[41–43] The local Coulomb interaction of the Yb 4*f* electrons was parameterized in terms of the Slater parameters F^0, F^2, F^4, and F^6. At the beginning of each LDA iteration, the parameters F^2, F^4, and F^6 were calculated through a radial integration of the unscreened local Coulomb interaction and then scaled by 0.95, 0.97, and 1.00, respectively.[44,45] The scaling constants accounted for the screening by the non-*f*-electrons. The final fully self-consistent values for both Yb_3Si_5 and Yb_3Ge_5 are $F^2 = 14.4\,\text{eV}$, $F^4 = 9.5\,\text{eV}$, and $F^6 = 7.0\,\text{eV}$, which shows that these higher order Slater parameters were rather insensitive to the chemical environment of the Yb atom. The Hubbard U parameter F^0 could not be calculated in the same way as it was too heavily screened. Instead, it was set to the constant value of 7.4 and 7.9 eV for Yb_3Si_5 and Yb_3Ge_5, respectively. The **k**-points were distributed in a $7 \times 7 \times 11$ Monkhorst–Pack grid with a shift of half a unit cell vector in the z-direction, and the Brillouin zone integration was carried out using Fermi smearing with $T = 273$ and 80 K.

The ED impurity solver takes some of the hybridization between the correlated *f*-orbitals and the rest of the material into account, by including a limited number of auxiliary bath orbitals in the impurity problem.[42] The total number of bath orbitals that can be included in the impurity problem is severely limited by the size of the many-body Hilbert space. The Hilbert space grows particularly fast if the added orbitals and electrons bring the total system, i.e., impurity and bath, closer to half-filling. This is the case if bath orbitals with negative binding energies are added to the almost-filled Yb impurity orbitals. In addition, the final states of a photoemission process are in general only weakly affected by the nominally unoccupied bath orbitals, as long as the repulsive Coulomb interaction is large compared to the hybridization strength.[46] This can be understood by noting that these final states have one less electron than the ground state. They would therefore increase their energy substantially if the impurity would donate an additional electron to the bath, which implies that their effective hybridization with the unoccupied bath states will be small.

In this study, we therefore included only nominally occupied bath states in the impurity problem, specifically those with binding energies larger than $4k_BT$, where k_B and T are Boltzmann constant and temperature, respectively. Under this constraint, the number of included bath orbitals is limited by the stability of the hybridization function fitting (including its off-diagonal elements) rather than by the Hilbert space size. This approach enabled us to include up to 40 nominally occupied bath spin–orbitals. The downside of excluding the low-energy bath states is that it makes it in general not possible to converge to a stable solution with a sizeable Kondo quasiparticle peak.

4. Results and Discussion

4.1 *Magnetic susceptibility*

Figures 2(a) and 2(b) show the temperature dependence of the magnetic susceptibility of Yb_3Si_5 and Yb_3Ge_5 (open circles), measured up to 300 K. The rapid increase in the magnetic susceptibility at low temperatures may be attributed to impurity contributions. Following corrections were applied to the measured susceptibility. (i) The low-temperature upturn in $\chi(T)$ was subtracted by a Curie–Weiss term. (ii) Diamagnetic contributions from the inner closed shell were subtracted to obtain the spin susceptibility. The diamagnetic values were taken from Ref. 47. In most cases, these diamagnetic contributions can be neglected. However, in the case of Yb_3Ge_5, the spin magnetic susceptibility was very small due to its nearly divalent state. Thus, the core diamagnetism needed to be explicitly considered. Finally, we obtained the corrected magnetic susceptibility as shown in Figs. 2(a) and 2(b) (open squares).

On the other hand, performing a Curie–Weiss fit for the magnetic susceptibility of Yb_3Ge_5 was challenging. Therefore, we fitted only the corrected data of Yb_3Si_5 for $T > 200\,\text{K}$.[48] In Yb_3Si_5 Curie constant and Weiss temperature were determined to be 2.29 emu/mol and -183 K, respectively. The effective magnetic moment of Yb_3Si_5 was estimated to be $4.28\mu_B$, which is close to the free Yb^{3+} ion value of $4.54\mu_B$. This suggests that Yb_3Si_5 is in a mixed-valence state, close to the trivalent configuration.

Based on the Bethe–Ansatz solution of the Coqblin–Schrieffer model, the physical properties of a Kondo system are scaled by a single parameter, the characteristic temperature T_0. Rajan solved the Coqblin–Schrieffer model numerically.[49] We fit the corrected magnetic susceptibility with T_0 as a fit parameter using the Rajan's curve as shown in Figs. 2(c) and 2(d) (dotted lines). Rajan showed that magnetic susceptibility at zero temperature, $\chi(0)$ and T_0 was related by $\chi(0) = N_A\nu(\nu^2 - 1)g\mu_B^2/(24\pi k_BT_0)$, where N_A, ν, g, and μ_B are Avogadro number, $\nu = 2J + 1$ (J: total angular momentum), Landé g-factor, and Bohr magneton, respectively. T_0 was estimated to be 509 K for Yb_3Si_5 and 1324 K for Yb_3Ge_5.

We also apply a theoretical universal curve based on the single-impurity Anderson model by Bickers et al.[50,51] for the corrected magnetic susceptibility, as shown in Figs. 2(c) and 2(d) (dashed lines). T_0 was estimated to be 584 K for Yb_3Si_5 and 2270 K for Yb_3Ge_5. Neither of these theoretical fits fully reproduces the experimental data, and the values of T_0 show significant discrepancies between the two models, particularly for Yb_3Ge_5. Since both models are based on a nearly Yb^{3+} state, this discrepancy may be reasonable given that the Yb valence in Yb_3Ge_5 is closer to Yb^{2+}. Nevertheless, both model fits indicate that the characteristic temperature of Yb_3Ge_5 is significantly higher than that of Yb_3Si_5.

T_0 is a measure of the Kondo temperature (T_K), suggesting that the Kondo temperature of Yb_3Ge_5 may be considerably higher than that of Yb_3Si_5. According to Kaga et al.,[52] the temperature at which the Kondo lattice was formed at $T_{coh} \sim 0.1T_K$. In Yb_3Si_5 the resistivity measurement indicates the formation of a Fermi liquid state at $T < 50$,[14] which may

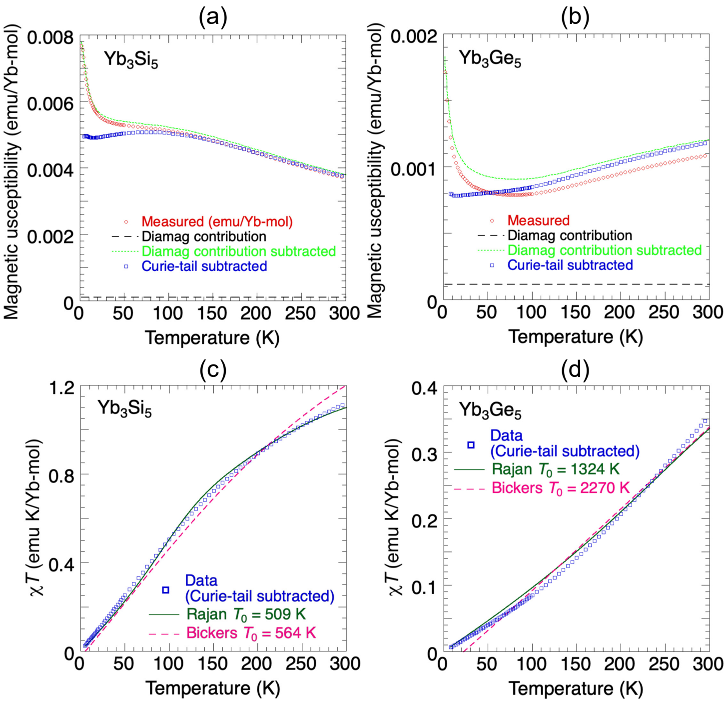

Fig. 2. (Color online) (a, b) Temperature dependence of the magnetic susceptibility (open circles) of (a) Yb_3Si_5 and (b) Yb_3Ge_5. We also show the diamagnetic contributions from the inner closed shell (dashed line),[47] the susceptibility subtracting the diamagnetic contribution (dotted line), and the susceptibility subtracting the Curie–Weiss term at low temperatures (open squares). (c, d) Rajan's model fit (solid line) and Bickers' model fit (dashed line) to χT (open circles) for (c) Yb_3Si_5 and (d) Yb_3Ge_5.[49–51]

correspond to T_{coh}. Thus, the value of T_0 for Yb_3Si_5 estimated from the model fit to the magnetic susceptibility appears reasonable.

Furthermore, we fitted the magnetic susceptibility using the ICF model, even though the conventional ICF model assumes two distinct valence states and does not account for crystal field effects, the chemical potential, or hybridization.[48] Here, we improved the ICF model by incorporating a temperature-dependent chemical potential.[48] The modified ICF model predicts a monotonic decrease in the Yb valence. However, the valence estimated by the improved ICF model exhibits an unrealistically strong temperature dependence, decreasing from 2.7 at 300 K to 2.2 at 0 K for Yb_3Si_5, and from 2.2 at 300 K to 2.0 at 0 K for Yb_3Ge_5, which is clearly incompatible with the PFY-XAS and RXES results shown below.

Grytsiv et al.[14,15] estimated the electronic specific heat (γ) to be approximately 30 mJ/(mol K^2) for Yb_3Si_5 and 20 mJ/(mol K^2) for Yb_3Ge_5 using the universal relation $A/\gamma^2 = 10^{-5}\,\mu\Omega\,\mathrm{cm(mol\,K/mJ)}^2$, where A is a coefficient of the temperature term T^2 in the temperature dependence of resistivity.[53] Additionally, Rajan[49] established a relation between T_0 and γ to be $T_0 = N_A(\nu - 1)\pi k_B/6\gamma$. γ is estimated to be 60 mJ/(mol K^2) for Yb_3Si_5 and 23 mJ/(mol K^2) for Yb_3Ge_5 assuming $J = 7/2$.

4.2 *Temperature dependence of the PFY-XAS and RXES spectra*

PFY-XAS and RXES spectra were measured to investigate the temperature dependence of the bulk Yb valence. These techniques offer a distinct advantage of being truly bulk sensitive, whereas UV and soft x-ray PES also pick up a sizable contribution from the surface and subsurface.[54] The RXES spectra were recorded at $h\nu = 8938$ eV, corresponding to the resonant energy of the Yb^{2+} component, and were normalized to the intensity of the Yb^{3+} peak. The results are presented in Figs. 3(a)–3(d).

The Yb valence, defined as $v = 3 - \eta$, is shown in Figs. 3(g) and 3(h). It was extracted from the measured intensity ratios (r) between the Yb^{3+} and Yb^{2+} components in the spectra using the relation, $\eta = \frac{1}{1+\frac{r}{\zeta}}$, with $\zeta = 1$ for PFY-XAS and $\zeta < 1$ for RXES, accounting for the reduced 3+ intensity in the latter. The PFY-XAS spectra were fitted assuming Voigt functions for the Yb^{n+} components with an arctan-like background as illustrated in Fig. 3(e). The intensities of the two arctan-like backgrounds were determined to be proportional to the intensities of their corresponding Voigt functions of the Yb^{2+} and Yb^{3+} components. An example of the fit for the RXES spectrum is shown in Fig. 3(f). We estimated that $\zeta = 0.267$ for Yb_3Si_5, and 0.178 for Yb_3Ge_5 by comparing the intensity ratios obtained from PFY-XAS and RXES spectra. The Yb valence of Yb_3Si_5 monotonically decreases with decreasing temperature below room temperature, while that of Yb_3Ge_5 remains nearly constant down to 23 K. The relatively constant valence of Yb_3Ge_5 suggests that its Kondo temperature is beyond the measured temperature range, likely well above room temperature. This finding supports the high characteristic temperatures derived from theoretical fits to the magnetic susceptibility.

4.3 *Pressure dependence of the PFY-XAS spectra and RXES spectra*

We also measured the pressure dependence of the PFY-XAS spectra of Yb_3Si_5 and Yb_3Ge_5 at room temperature as shown in Figs. 4(a) and 4(b), respectively. Pressure

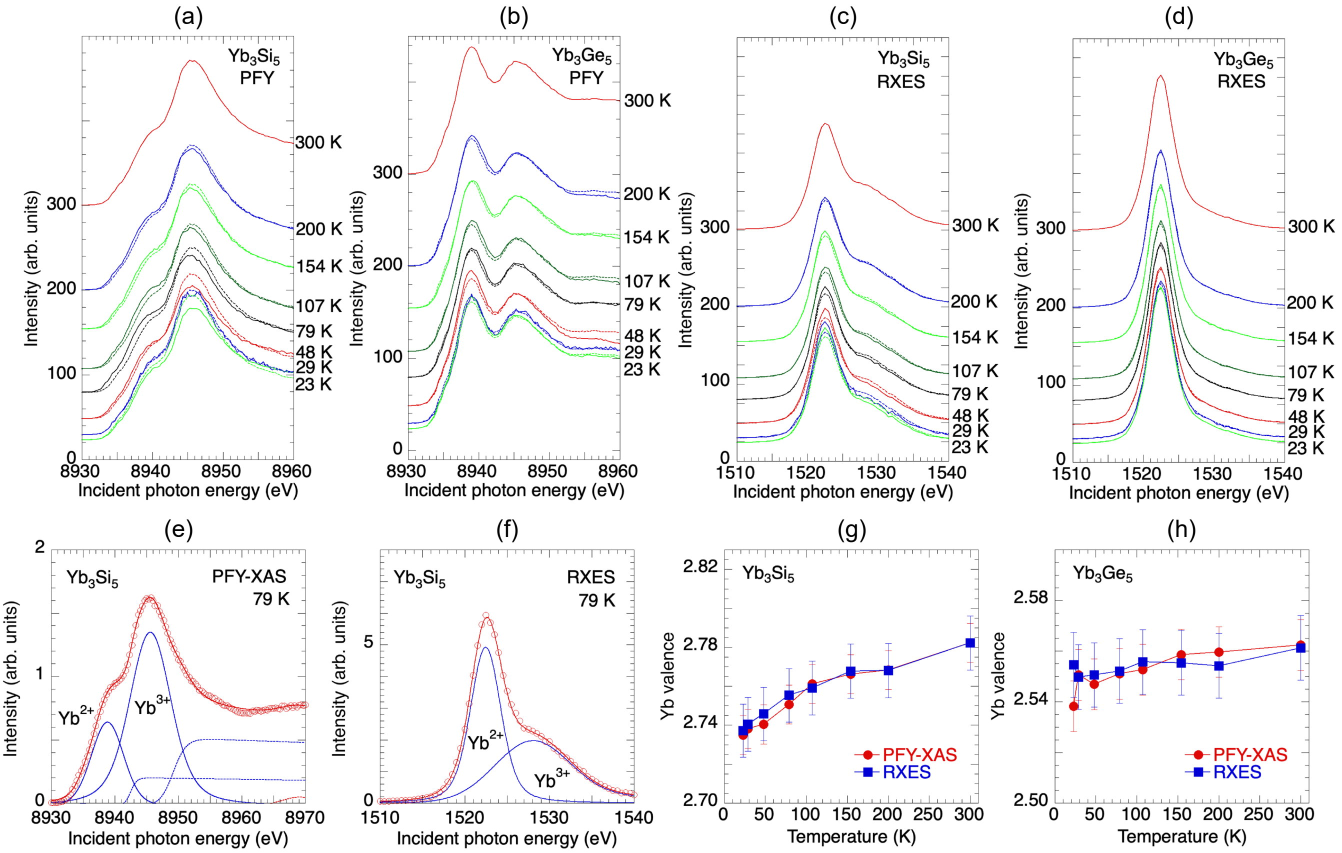

Fig. 3. (Color online) (a, b) PFY-XAS spectra at the Yb-L_3 absorption edge for (a) Yb_3Si_5 and (b) Yb_3Ge_5 as a function of temperature. The spectra with dotted lines at 300 K are shown overlapping the spectrum at a given temperature of less than 200 K. (c, d) RXES spectra for (c) Yb_3Si_5 and (d) Yb_3Ge_5 at the incident photon energy of 8938 eV as a function of temperature. The spectra with dotted lines at 300 K are shown overlapping the spectrum at a given temperature of less than 200 K. (e, f) Fit examples (solid and dashed lines) of (e) the PFY-XAS and (f) RXES spectra for Yb_3Si_5 at 79 K. Open circles in (e) and (f) are experimental data. (g, h) Yb valence of Yb_3Si_5 and Yb_3Ge_5.

dependences of the Yb valence estimated from the fits to the PFY-XAS spectra are presented in Figs. 4(c) and 4(d) for Yb_3Si_5 and Yb_3Ge_5, respectively.[26–28] The pressure dependence of the Yb valence was fitted using a modified logistic function as shown by the solid lines in Figs. 4(c) and 4(d). We define the critical pressure, P_v as the pressure corresponding to the peak of the differential of the fitted curve (dashed line).[55]

In Yb_3Si_5 the Yb valence gradually increased with pressure from approximately 2.77 at ambient pressure to 2.8 at 25 GPa. In Yb_3Ge_5 the Yb valence also increased gradually from approximately 2.54 at ambient pressure to 2.66 at 20 GPa. However, further increases in pressure beyond 20 GPa did not result in significant changes in the Yb valence within the measured pressure range. The pressure-induced change in the Yb valence was relatively small in Yb_3Si_5, on the order of 0.03, whereas in Yb_3Ge_5, it was significantly larger, on the order of 0.12. Since the Yb valence in Yb_3Si_5 is already 2.77 at room temperature, further changes induced by pressure may be minimal.

The critical pressures were determined to be $P_v = 10$–12 GPa for Yb_3Si_5 and $P_v = 8$–9 GPa for Yb_3Ge_5. In Yb_3Si_5 Muramatsu et al.[16] reported a minimum in the characteristic temperature (T^*) at around 21 GPa based on the electrical resistivity measurements under pressure. Here, T^* was defined as the temperature at which the temperature derivative of resistance exhibited a maximum. The increase of T^* is normally expected to lead to a decrease in the Yb valence. However, as shown in Fig. 4(c), no such behavior is observed in the pressure dependence of the Yb valence above 21 GPa. Instead, the Yb valence appears to saturate in this pressure range. It should be noted that the current Yb-valence measurement was conducted at room temperature, whereas the minimum of T^* in the electrical resistivity measurements was observed at low temperatures. Our previous studies revealed an anomalous pressure-induced decrease in Yb valence in $YbCu_5$,[56] with this behavior becoming more pronounced at lower temperatures. Therefore, future studies measuring the pressure dependence of the Yb valence in Yb_3Si_5 at low temperatures would be of great interest.

The Yb valence and the Kondo temperature are very different between Yb_3Si_5 and Yb_3Ge_5. One possible reason is that the lattice volumes of Yb_3Si_5 and Yb_3Ge_5 are different. Yb_3Si_5 is more likely to have a stronger Yb^{3+} due to the application of chemical pressure. However, the Yb valence of Yb_3Ge_5 at high pressure saturated at 20 GPa or higher, and did not reach the value of Yb_3Si_5 at ambient pressure. Therefore, the difference between them cannot be explained by chemical pressure alone. A possible interpretation is that the 4*s*, 4*p*, and/or 3*d* orbitals of Ge in Yb_3Ge_5 may be strongly hybridized with Yb-4*f*. However, the binding energy of the Ge *d* band is large and very deep, and the strong hybridization between Yb 4*f* and Ge 3*d* orbitals is unlikely. At present, the plausible reason of the above difference is unclear.

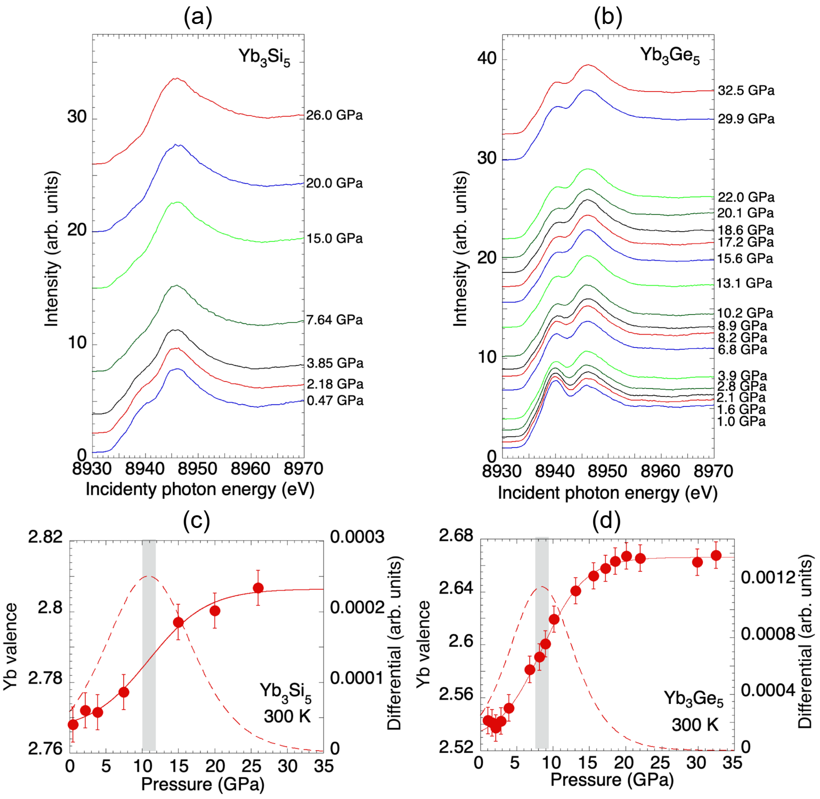

Fig. 4. (Color online) (a, b) PFY-XAS spectra for (a) Yb_3Si_5 and (b) Yb_3Ge_5 at the Yb-L_3 absorption edge as a function of pressure at room temperature. The baseline height of each spectrum corresponds to the measured pressure. (c, d) Pressure dependence of the Yb valence for (c) Yb_3Si_5 and (d) Yb_3Ge_5 (closed circles). Solid lines are fit curves with a modified logistic function. Dashed lines are differential of the fit curves. Grey areas are the inflection pressures of the fit curves, corresponding to the critical pressure (P_v).

4.4 Photoelectron spectroscopy

While PFY-XAS and RXES provide excellent bulk sensitivity, their energy resolution is limited due to the short lifetimes of core holes. In contrast, UV PES and SX PES offer much higher energy resolution but are highly surface-sensitive. The electron mean free path in Yb_3Si_5 and Yb_3Ge_5 is estimated to be approximately ~2 Å at $h\nu = 40$ eV.[57,58] At $h\nu = 172$ eV the escape depth increases to ~3 Å.

4.4.1 Temperature dependence

Figures 5(a) and 5(c) show the full valence band spectra of Yb_3Si_5 and Yb_3Ge_5 measured at $h\nu = 40$ eV between 9 to 250 K. The valence band spectra exhibit contributions from both Yb $4f^{14} \rightarrow 4f^{13}$ transitions (Yb^{2+}), between 0 to 3 eV, and Yb $4f^{13} \rightarrow 4f^{12}$ transitions (Yb^{3+}) between 5 to 12 eV.

The valence band spectrum of Yb_3Si_5 exhibits a stronger and more non-uniform temperature dependence. The Yb^{3+} component in Fig. 5(a) remains almost constant with temperature, except for the ^3F multiplet at 7.75 eV which slightly decreases in intensity as the temperature is lowered. In contrast, the Yb^{2+} component exhibits a more pronounced temperature dependence, as shown in Fig. 5(b). The Yb $^2F_{7/2}$ multiplet, centered at around 0.15 eV, also changes its shape with spectral weight shifting into a narrow region around 0.05 eV in the binding energy. Additionally, the Yb^{2+} surface components at 1.0 and 2.5 eV are enhanced with increasing temperature and shift slightly toward higher binding energy. The valence band spectrum of Yb_3Ge_5 also features two Yb $^2F_{7/2}$ and $^2F_{5/2}$ multiplet peaks at 0.12 and 1.4 eV. Both peaks increase uniformly in intensity as the

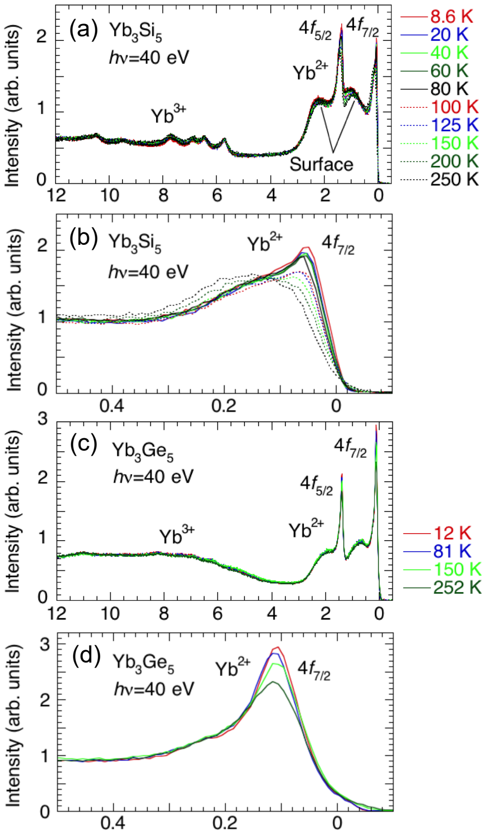

Fig. 5. (Color online) (a) Temperature dependence of the valence band spectra at $h\nu = 40$ eV for Yb_3Si_5. (b) Expanded view of the spectra in (a) near the Fermi level. (c) Temperature dependence of the valence band spectra at $h\nu = 40$ eV for Yb_3Ge_5. (d) Expanded view of the spectra in (c) near the Fermi level.

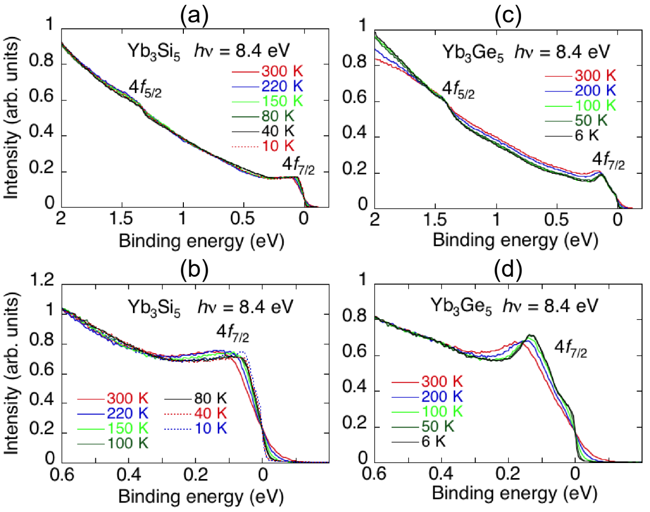

Fig. 6. (Color online) (a) Temperature dependence of the high-resolution valence band spectra at $h\nu = 8.4\,\mathrm{eV}$ (Xe lamp) for Yb_3Si_5. (b) Expanded view of the spectra in (a) near the Fermi level. (c) Temperature dependence of the high-resolution valence band spectra at $h\nu = 8.4\,\mathrm{eV}$ (Xe lamp) for Yb_3Ge_5. (d) Expanded view of the spectra in (c) near the Fermi level.

temperature decreases as the temperature is lowered, as shown in Fig. 5(d).

Figure 6 shows photoelectron spectra obtained using a Xe lamp ($h\nu = 8.4\,\mathrm{eV}$) with an energy resolution of less than 10 meV, allowing for the resolution of spectral features near the Fermi energy. Although the photoionization cross-section of the 4f electrons is low, as evidenced by the small weight of the Yb $^2F_{5/2}$ multiplet at 1.4 eV, the Yb $^2F_{7/2}$ multiplet remains visible. The Yb_3Si_5 spectrum in Fig. 6(b) exhibits an overall temperature dependence similar to that observed at $h\nu = 40\,\mathrm{eV}$. In contrast, the Yb_3Ge_5 spectrum in Fig. 6(d) shows a reduced broadening of the $^2F_{7/2}$ multiplet at low temperatures. Additionally, the peak intensity at 0.13 eV in Yb_3Ge_5 is stronger than that at 0.05 eV in Yb_3Si_5. The peaks at 0.05 eV (Yb_3Si_5) and 0.13 eV (Yb_3Ge_5) can be identified as Kondo resonance peaks. This directly demonstrates that Yb_3Si_5 and Yb_3Ge_5 are the Kondo-lattice compounds and that the Kondo temperature of Yb_3Ge_5 is significantly higher than that of Yb_3Si_5. This would explain the nearly constant Yb valence of Yb_3Ge_5 over the measured temperature range, as shown in Fig. 3. This conclusion is further supported by the model fit results for the magnetic susceptibility of Yb_3Si_5 and Yb_3Ge_5.

4.4.2 Spectral decomposition

Figures 7(a), 7(b), and 7(c) show the valence band spectra of Yb_3Si_5 and Yb_3Ge_5 near the Fermi level, measured at $h\nu =$ 9.9–40 eV and at temperatures of 9–10 K. The corresponding fitted valence band spectra are presented in Figs. 7(d) and 7(e). Abbati et al.[19,21] previously fitted the valence band spectrum of Yb_3Si_5 using three pairs of spin–orbit split peaks, attributing them to the surface, subsurface, and bulk contributions, in descending order of binding energy, analogous to $YbAl_2$.[59] However, a closer inspection of our high-resolution measurements in Figs. 7(a)–7(c) reveals that the main peaks are best described by two separate spin–orbit split contributions. Additionally, the broad spectral features around 0.75 and 2 eV each consist of two peaks. Hereafter, we designate the pair of spin–orbit split peaks at the lowest binding energy bulk peaks, the pair at higher binding energy subpeaks, and the remaining two pairs as surface peaks, as illustrated in Figs. 7(d) and 7(e). All these components are also present in the spectra recorded at $h\nu = 172$ and 174 eV, presented in Figs. 9(a) and 9(c), albeit with significantly different intensities. A similar subpeak structure has also been assumed in the fitting of valence band spectra for $YbInCu_4$[60] and $YbAl_3$.[61] The subpeaks may either originate from bulk contributions due to final-state effects or be related to surface and subsurface states.[62,63] We will investigate the role of the final state effects using LDA+DMFT in Sect. 5, while the contribution of the surface and subsurface will be the focus of the rest of this section.

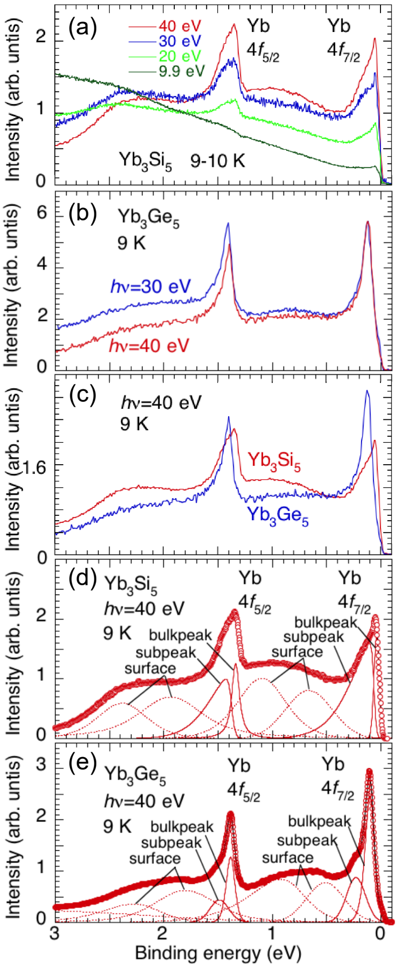

Fig. 7. (Color online) Valence band spectra taken at $h\nu < 40\,\mathrm{eV}$. (a) Valence band spectra near the Fermi level at 9–10 K and $h\nu = 9.9$, 20, 30, and 40 eV for Yb_3Si_5. (b) Valence band spectra at 9 K and $h\nu = 30$ and 40 eV for Yb_3Ge_5. (c) Comparison of the valence band spectra between Yb_3Si_5 and Yb_3Ge_5 at 9 K and $h\nu = 40\,\mathrm{eV}$. (d, e) Examples of the fits (solid and dashed lines) to the experimental valence band spectra (open circles) at 9 K for (d) Yb_3Si_5 and (e) Yb_3Ge_5.

We first examine the assignment of the broad surface peaks. Their binding energies are approximately 1 eV higher than those of the corresponding bulk peaks, which is typical for Yb^{2+} surface atoms.[64] Furthermore, their peak widths are more than three times larger than those of the bulk peaks, indicating a distinctly different chemical environment. In addition, they exhibit the same reduction in intensity relative to the bulk peaks when moving from $h\nu = 40\,\mathrm{eV}$ to the more bulk sensitive $h\nu = 172\,\mathrm{eV}$. The two separate surface

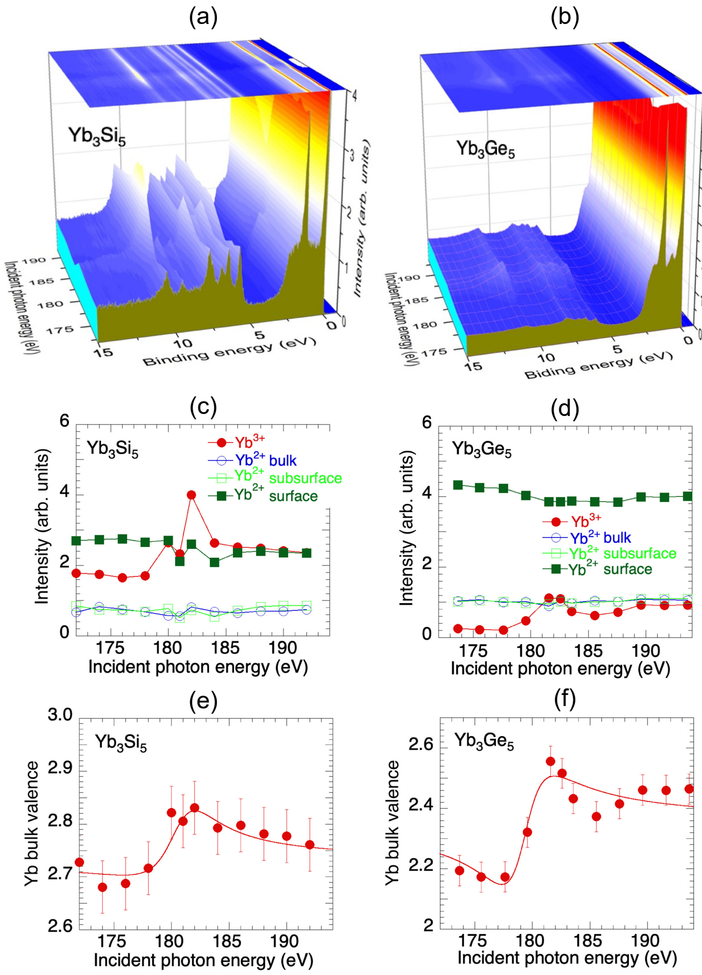

Fig. 8. (Color online) Yb $4d$–$4f$ resonant photoelectron spectra of the valence band for Yb_3Si_5 and Yb_3Ge_5 at 9 K. Solid lines are the fits with the Fano-like profiles. (a, b) Resonant photoelectron spectra of the valence band as a function of the incident energies for (a) Yb_3Si_5 and (b) Yb_3Ge_5. (c, d) Change in the intensity of each Yb component around the resonant photon energies. Note that two surface components for the $4f_{7/2}$ bulk peak are denoted as surface and subsurface. (e, f) Change in the deduced Yb bulk valence around the resonant photon energies.

components may correspond to the bulk and subpeak, respectively. The presence of two separate surface components is consistent with a cleaved polycrystalline sample of a layered material. The bulk peaks are sharp and have binding energies consistent with an intermediate Yb valence. While the narrow peaks near the Fermi level exhibit characteristics of a Kondo resonance, they also have a spin–orbit split counterpart at binding energy 1.3 eV higher, which displays a very similar temperature dependence.

4.4.3 Resonant PES

The resonant valence-band spectra were measured as a function of the incident photon energies at the Yb-$4d$ absorption edge for both compounds, as shown in Fig. 8(a) for Yb_3Si_5 and Fig. 8(b) for Yb_3Ge_5 at 9 K. The intensity is normalized to the intensity of the surface Yb^{2+} component. Figures 8(c) and 8(d) display the intensity of each component as a function of the incident photon energies. As seen in Figs. 8(a)–8(d), a selective enhancement of the Yb^{3+} peaks at 11.5 eV (^3P), 11 eV (^1I), and 6 eV (^3H) occurs around $h\nu = 182$ eV due to a resonant $4d$–$4f$ emission process, similar to observations in other Yb compounds.[45] The electron emission process involves two distinct channels: direct photoionization and a super Coster–Kronig Auger decay, expressed respectively as

$$h\nu + 4d^{10}4f^{13} \rightarrow 4d^{10}4f^{12}\epsilon l + e_k,$$

$$h\nu + 4d^{10}4f^{13} \rightarrow 4d^{9}4f^{14} \rightarrow 4d^{10}4f^{12}\epsilon l + e_k,$$

where $h\nu$ denotes the incoming photon and e_k the emitted electron.[44,65,66] $4d^9 4f^{14}$ and $4d^{10}4f^{12}\epsilon l$ are the discrete and continuum states, respectively, and the Fano profile can be observed if the interaction occurs between these states. A Fano-like profile[67] is observed in the Yb^{3+} intensity in Figs. 8(c) and 8(d) due to the quantum interference between the two channels.

The Yb valence estimated from the ratio of the Yb^{3+} and Yb^{2+} components at each photon energy is plotted in Figs. 8(e) and 8(f). In these figures, two surface-related components for the $4f_{7/2}$ bulk peak are labeled as surface and subsurface. To obtain an accurate Yb valence, the ratio should be evaluated well before the resonance regime, as the Auger decay selectively enhances the Yb^{3+} signal. Using this approach, the Yb valence is determined to be 2.7 for Yb_3Si_5 and 2.2 for Yb_3Ge_5. Interestingly, the low-temperature Yb valences of 2.75 for Yb_3Si_5 and 2.54 for Yb_3Ge_5, obtained from the PFY-XAS spectra, are closer to the estimated valence values in Figs. 8(e) and 8(f) immediately after the resonance. This discrepancy between the results from XAS and PES is not unique to Yb_3Si_5 and Yb_3Ge_5 but has been observed in several other materials as well.[54,68,69] Further-

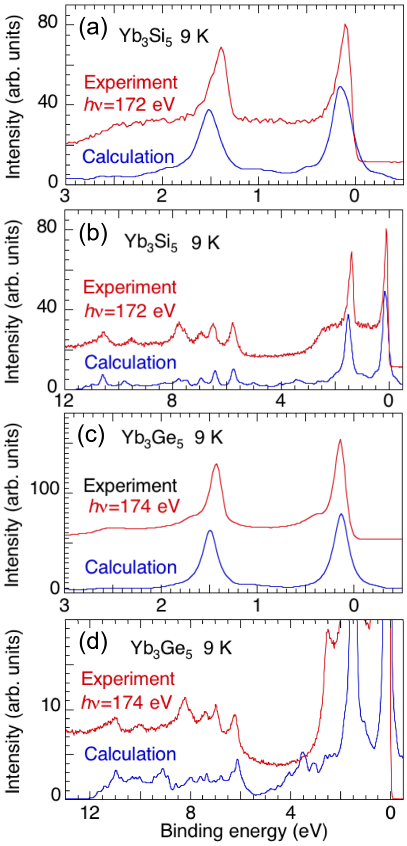

Fig. 9. (Color online) (a, c) Valence band spectra near the Fermi level at 9 K and $h\nu = 172, 174$ eV (at off-resonance) for (a) Yb_3Si_5 and (c) Yb_3Ge_5 with the LDA+DMFT calculated results of the total DOS. (b, d) Full valence band spectra are shown in (b) for Yb_3Si_5 and (d) for Yb_3Ge_5.

more, none of the Yb^{2+} components, including the surface and subsurface contributions, exhibit resonant behavior.

5. LDA+DMFT Calculations

Here, we discuss the subpeaks and the role of the final-state effects. The identification of the Yb^{2+} components in Sect. 4.4.2 (Spectral decomposition) assumes that the spectrum is composed of atomic-like $^2F_{7/2}$ multiplet peaks. Although the strong contraction of the Yb $4f$ orbitals reduces their hybridization and the neighboring orbitals small, the shape and cross sections of the multiplet peaks may still be influenced. Several fully-charge self-consistent LDA+DMFT calculations were performed in order to probe the orbital character of the bulk states and elucidate the role of possible final-state effects.

Figure 9 compares spectral densities calculated using LDA+DMFT with the experimentally measured valence band spectra. Overall, the theory reproduces the bulk component of the experimental spectra well for both Yb_3Si_5 and Yb_3Ge_5. There are indications of final-state effects in the theoretical spectra, such as small shoulder peaks in the region where the subpeaks are located. However, the intensity of these calculated peaks is significantly lower than that of the experimental subpeaks. An analysis of the excited many-body states in the impurity problem reveals that these peaks in the spectral density correspond to an almost complete transfer of an electron from the lowest-lying bath state to the Yb atom. Since the hybridization function is relatively flat around the Fermi energy in both Yb_3Si_5 and Yb_3Ge_5, incorporating additional low-energy bath states into the impurity problem would result in a smoothly decaying tail of the main peak rather than distinct side peaks. This supports the interpretation that the subpeaks originate from subsurface states rather than final-state effects.

6. Conclusion

The PFY-XAS and RXES measurements revealed that the Yb valence of Yb_3Si_5 decreases slightly with decreasing temperature below room temperature. In contrast, in Yb_3Ge_5, it was almost temperature-independent down to 23 K. This temperature-dependent behavior in Yb_3Si_5 corresponds well to the Fermi liquid formation at $T < 50$ K. These results, combined with the model fit results for the magnetic susceptibility, suggest that the Kondo temperature of Yb_3Ge_5 is significantly higher than that of Yb_3Si_5.

A high-resolution PES study demonstrated a clear increase in the intensity of the $4f_{7/2}$ component at the Fermi level in Yb_3Si_5 and Yb_3Ge_5 with decreasing the temperature, indicating the presence of the Kondo resonance peak of Yb_3Si_5. Additionally, high-resolution photoemission revealed extra Yb^{2+}-derived subpeaks, which are likely closely related to the layered structure of the materials. To confirm these findings, further studies on single crystals will be necessary. For example, an STM study of a freshly cleaved sample could provide insights into surface reconstruction and the presence of a double surface signal. Yb $4d$–$4f$ resonant PES showed a resonant enhancement of the Yb^{3+} intensity for both compounds, which can be described using the Fano-like profiles.

High-pressure study for Yb_3Si_5 and Yb_3Ge_5 revealed the pressure-induced successive transition of the Yb valence toward the Yb^{3+} state. Critical pressures for the valence transition were estimated to be approximately 10–12 GPa for Yb_3Si_5 and 8–9 GPa for Yb_3Ge_5.

Fully-charge self-consistent LDA+DMFT calculations were performed to investigate the bulk component of the spectra and elucidate the role of final-state effects. Overall, the theory reproduced the bulk component of the experimental spectra well as a whole for both Yb_3Si_5 and Yb_3Ge_5.

Acknowledgments We thank Hirokazu Hayashi, Jian Jiang, and Hideaki Iwasawa for their help in the experiments at HiSOR. The experiments were performed at HiSOR beamlines BL-1 and BL-9A (HiSOR under Proposals Nos. 11-A-10, 12-A-1, and 16AG003) in Hiroshima University and SPring-8 Taiwan beamline BL12XU under SPring-8 Proposals Nos. 2011B4260, 2018A41258, and 2023B4267, corresponding NSRRC Proposals Nos. 2011-2-021, 2018-1-012, and 2024-1-003. We thank N-BARD, Hiroshima University for supplying the liquid helium. This work is supported by JSPS KAKENHI (Grants-in-Aid for Scientific Research), Grant Numbers 24K00590 and 24K21692.

---

[*] Corresponding author. E-mail: hitoshi_yamaoka@mineo.jp

[†] Corresponding author. E-mail: patrik.thunstrom@physics.uu.se

[‡] Present address: Institute of Physics, Experimental Physics VII, University of Würzburg, Am Hubland, 97074 Würzburg, Germany

1) P. Wachter, in *Handbook on the Physics and Chemistry of Rare Earths*, ed. K. A. Gschneidner, Jr., L. Eyring, G. H. Lander, and G. R. Chopin (North-Holland, Amsterdam, 1994) Vol. 19, p. 177.
2) E. Bauer, Adv. Phys. **40**, 417 (1991).
3) J. Lawrence, Mod. Phys. Lett. B **22**, 1273 (2008).
4) F. Ahmed, J. Valenta, N. Tsujii, A. Hussain, N. Jabeen, and T. Mori, Mater. Res. Express **8**, 075504 (2021).
5) K. Kuga, K. Hirata, M. Matsunami, and T. Takeuchi, Appl. Phys. Lett. **123**, 202201 (2023).
6) T. Ishiyama, T. Ozawa, N. Saitoh, N. Yoshizawa, T. Suemasu, and K.

Toko, APL Mater. **12**, 021119 (2024).
7) K. N. Tu, R. D. Thompson, and B. Y. Tsaur, Appl. Phys. Lett. **38**, 626 (1981).
8) S. Zhu, J. Chen, M. F. Li, S. J. Lee, J. Singh, C. X. Zhu, A. Du, C. H. Tung, A. Chin, and D. L. Kwong, IEEE Electron Device Lett. **25**, 565 (2004).
9) K. Kuga, M. Matsunami, H. Fujiwara, G. Nozue, A. Ose, A. Sekiyama, A. Yasui, S. Hamamoto, M. Oura, and T. Takeuchi, Jpn. J. Appl. Phys. **62**, SD1014 (2023).
10) A. Iandelli, A. Palenzona, and G. L. Olcese, J. Less-Common Met. **64**, 213 (1979).
11) G. S. Smith, Q. Johnson, and A. G. Tharp, Acta Crystallogr. **18**, 1085 (1965).
12) G. Balducci, S. Brutti, A. Ciccioli, G. Gigli, A. Palenzona, and M. Pani, J. Phys. Chem. B **111**, 5132 (2007).
13) B. C. Sales and D. K. Wohlleben, Phys. Rev. Lett. **35**, 1240 (1975).
14) A. Grytsiv, D. Kaczorowski, A. Leithe-Jasper, V. H. Tran, A. P. Pikul, P. Rogl, M. Potel, H. Noël, and T. Velikanova, J. Solid State Chem. **163**, 178 (2002).
15) A. Grytsiv, D. Kaczorowski, A. Leithe-Jasper, P. Rogl, M. Potel, H. Noël, A. P. Pikul, and T. Velikanova, J. Solid State Chem. **165**, 178 (2002).
16) T. Muramatsu, T. Kagayama, K. Shimizu, D. Kaczorowski, A. Grytsiv, and P. Rogl, J. Magn. Magn. Mater. **310**, e25 (2007).
17) I. Abbati, L. Braicovich, U. del Pennino, A. Iandelli, G. L. Olcese, A. Plalenzona, C. Carbone, J. Nogami, J. J. Yeh, and I. Lindau, Physica B+C **130**, 141 (1985).
18) I. Abbati, L. Braicovich, B. De Michelis, A. Fasana, M. Sancrotti, A. Landelli, G. L. Olcese, and A. Palenzona, J. Less-Common Met. **120**, L1 (1986).
19) I. Abbati, L. Braicovich, U. del Pennino, C. Carbone, J. Nogami, J. J. Yeh, I. Lindau, A. Iandelli, G. L. Olcese, and A. Plalenzona, Phys. Rev. B **34**, 4150 (1986).
20) L. Braicovich, Thin Solid Films **140**, 79 (1986).
21) I. Abbati, L. Braicovich, C. Carbone, J. Nogami, I. Lindau, A. Iandelli, G. L. Olcese, and A. Plalenzona, Solid State Commun. **62**, 35 (1987).
22) R. Pöttgen, R.-D. Hoffmann, and D. Kußmann, Z. Anorg. Allg. Chem. **624**, 945 (1998).
23) V. Babizhetskyy, V. Levytskyy, R. Jardin, J. Bauer, R. Guérin, R. Gautier, B. Fontaine, and J.-F. Halet, Z. Anorg. Allg. Chem. **646**, 1168 (2020).
24) K. S. Chi, W. C. Tsai, and L. J. Chen, J. Appl. Phys. **93**, 153 (2003).
25) C. Wigren, J. N. Andersen, R. Nyholm, and U. O. Karlsson, J. Vac. Sci. Technol. A **9**, 1942 (1991).
26) H. Yamaoka, I. Jarrige, N. Tsujii, N. Hiraoka, H. Ishii, and K.-D. Tsuei, Phys. Rev. B **80**, 035120 (2009).
27) H. Yamaoka, I. Jarrige, N. Tsujii, J.-F. Lin, N. Hiraoka, H. Ishii, and K.-D. Tsuei, Phys. Rev. B **82**, 035111 (2010).
28) H. Yamaoka, I. Jarrige, N. Tsujii, J.-F. Lin, T. Ikeno, Y. Isikawa, K. Nishimura, R. Higashinaka, H. Sato, N. Hiraoka, H. Ishii, and K.-D. Tsuei, Phys. Rev. Lett. **107**, 177203 (2011).
29) H. K. Mao and P. M. Bell, Science **191**, 852 (1976).
30) K. Syassen, High Pressure Res. **28**, 75 (2008).
31) H. Yamaoka, High Pressure Res. **36**, 262 (2016).
32) K. Shimada, M. Arita, Y. Takeda, H. Fujino, K. Kobayashi, T. Narimura, H. Namatame, and M. Taniguchi, Surf. Rev. Lett. **9**, 529 (2002).
33) M. Arita, K. Shimada, Y. Takeda, M. Nakatakle, H. Namatame, and M. Taniguchi, Surf. Rev. Lett. **9**, 535 (2002).
34) H. Yamaoka, Y. Yamamoto, E. F. Schwier, F. Honda, Y. Zekko, Y. Ohta, J.-F. Lin, M. Nakatake, H. Iwasawa, M. Arita, K. Shimada, N. Hiraoka, H. Ishii, K.-D. Tsuei, and J. Mizuki, Phys. Rev. B **92**, 235110 (2015).
35) A. Georges, G. Kotliar, W. Krauth, and M. J. Rozenberg, Rev. Mod. Phys. **68**, 13 (1996).
36) G. Kotliar, S. Y. Savrasov, K. Haule, V. S. Oudovenko, O. Parcollet, and C. A. Marianetti, Rev. Mod. Phys. **78**, 865 (2006).
37) J. Wills, O. Eriksson, M. Alouani, and D. Price, in *Electronic Structure and Physical Properties of Solids*, ed. H. Dreysse (Springer, New York, 2000) p. 148.
38) A. Grechnev, I. Di Marco, M. I. Katsnelson, A. I. Lichtenstein, J. Wills, and O. Eriksson, Phys. Rev. B **76**, 035107 (2007).
39) I. Di Marco, J. Minár, S. Chadov, M. I. Katsnelson, H. Ebert, and A. I. Lichtenstein, Phys. Rev. B **79**, 115111 (2009).
40) P. Thunström, I. Di Marco, A. Grèchnev, S. Lebegue, M. I. Katsnelson, A. Svane, and O. Eriksson, Phys. Rev. B **79**, 165104 (2009).
41) P. Thunström, I. Di Marco, and O. Eriksson, Phys. Rev. Lett. **109**, 186401 (2012).
42) M. Caffarel and W. Krauth, Phys. Rev. Lett. **72**, 1545 (1994).
43) A. Liebsch and H. Ishida, J. Phys.: Condens. Matter **24**, 053201 (2012).
44) H. Yamaoka, P. Thunström, I. Jarrige, K. Shimada, N. Tsujii, M. Arita, H. Iwasawa, H. Hayashi, J. Jian, T. Habuchi, D. Hirayama, H. Namatame, M. Taniguchi, U. Murao, S. Hosoya, A. Tamaki, and H. Kitazawa, Phys. Rev. B **85**, 115120 (2012).
45) H. Yamaoka, P. Thunström, N. Tsujii, I. Jarrige, K. Shimada, M. Arita, H. Iwasawa, H. Hayashi, J. Jiang, H. Namatame, M. Taniguchi, N. Hiraoka, H. Ishii, K.-D. Tsuei, M. Giovannini, and E. Bauer, Phys. Rev. B **86**, 085137 (2012).
46) M. Costa, P. Thunström, I. Di Marco, A. Bergman, A. B. Klautau, A. I. Lichtenstein, M. I. Katsnelson, and O. Eriksson, Phys. Rev. B **87**, 115142 (2013).
47) L. B. Mendelsohn, F. Biggs, and J. B. Mann, Phys. Rev. A **2**, 1130 (1970).
48) (Supplemental Material) Curie–Weiss fit for Yb_3Si_5, conventional ICF model, and details of the modified ICF model.
49) V. T. Rajan, Phys. Rev. Lett. **51**, 308 (1983).
50) N. E. Bickers, D. L. Cox, and J. W. Wilkins, Phys. Rev. B **36**, 2036 (1987).
51) N. E. Bickers, Rev. Mod. Phys. **59**, 845 (1987).
52) H. Kaga, H. Kubo, and T. Fujiwara, Phys. Rev. B **37**, 341 (1988).
53) K. Kadowaki and S. B. Woods, Solid State Commun. **58**, 507 (1986); N. Tsujii, H. Kontani, and K. Yoshimura, Phys. Rev. Lett. **94**, 057201 (2005); Note that the Kadowaki–Woods ratio A/γ^2 is 0.4×10^{-6} for $J = 7/2$. Therefore, γ for $J = 7/2$ is estimated to be approximately 165 mJ/(mol K^2) for Yb_3Si_5 and 100 mJ/(mol K^2) for Yb_3Ge_5.
54) K. Kummer, Yu. Kucherenko, S. Danzenbächer, C. Krellner, C. Geibel, M. G. Holder, L. V. Bekenov, T. Muro, Y. Kato, T. Kinoshita, S. Huotari, L. Simonelli, S. L. Molodtsov, C. Laubschat, and D. V. Vyalikh, Phys. Rev. B **84**, 245114 (2011).
55) H. Yamaoka, Y. Michiue, Y. Yamamoto, N. Tsujii, M. Arita, H. Sato, M. Sawada, H. Ishii, N. Hiraoka, and J. Mizuki, Phys. Rev. B **110**, 205129 (2024).
56) H. Yamaoka, N. Tsujii, M. Suzuki, Y. Yamamoto, I. Jarrige, H. Sato, J.-F. Lin, T. Mito, J. Mizuki, H. Sakurai, O. Sakai, N. Hiraoka, H. Ishii, K.-D. Tsuei, M. Giovannini, and E. Bauer, Sci. Rep. **7**, 5846 (2017).
57) M. P. Seah and W. A. Dench, Surf. Interface Anal. **1**, 2 (1979).
58) J. J. Yeh and I. Lindau, At. Data Nucl. Data Tables **32**, 1 (1985).
59) G. Kaindl, B. Reihl, D. E. Eastman, R. A. Pollak, N. Mårtensson, B. Barbara, T. Penney, and T. S. Plaskett, Solid State Commun. **41**, 157 (1982).
60) H. Sato, K. Yoshikawa, K. Hiraoka, M. Arita, K. Fujimoto, K. Kojima, T. Muro, Y. Saitoh, A. Sekiyama, S. Suga, and M. Taniguchi, Phys. Rev. B **69**, 165101 (2004).
61) S. Suga, A. Sekiyama, S. Imada, A. Shigemoto, A. Yamasaki, M. Tsunekawa, C. Dallera, L. Braicovich, T.-L. Lee, O. Sakai, S. Ebihara, and Y. Ōnuki, J. Phys. Soc. Jpn. **74**, 2880 (2005).
62) G. K. Wertheim, D. M. Riffe, N. V. Smith, and P. H. Citrin, Phys. Rev. B **46**, 1955 (1992).
63) S. Suga, A. Sekiyama, S. Imada, J. Yamaguchi, A. Shigemoto, A. Irizawa, K. Yoshimura, M. Yabashi, K. Tamasaku, A. Higashiya, and T. Ishikawa, J. Phys. Soc. Jpn. **78**, 074704 (2009).
64) S. Suga and A. Sekiyama, J. Electron Spectrosc. Relat. Phenom. **114–116**, 659 (2001).
65) H. Yamaoka, N. Tsujii, K. Yamamoto, H. Oohashi, A. M. Vlaicu, K. Kunitani, K. Uotani, D. Horiguchi, T. Tochio, Y. Ito, and S. Shin, Phys. Rev. B **76**, 075130 (2007).
66) H. Yamaoka, M. Matsunami, R. Eguchi, Y. Ishida, N. Tsujii, Y. Takahashi, Y. Senba, H. Ohashi, and S. Shin, Phys. Rev. B **78**, 045125 (2008).
67) U. Fano, Phys. Rev. **124**, 1866 (1964).
68) L. Moreschini, C. Dallera, J. J. Joyce, J. L. Sarrao, E. D. Bauer, V. Fritsch, S. Bobev, E. Carpene, S. Huotari, G. Vankó, G. Monaco, P. Lacovig, G. Panaccione, A. Fondacaro, G. Paolicelli, P. Torelli, and M. Grioni, Phys. Rev. B **75**, 035113 (2007).
69) Y. Utsumi, H. Sato, S. Ohara, T. Yamashita, K. Mimura, S. Motonami, K. Shimada, S. Ueda, K. Kobayashi, H. Yamaoka, N. Tsujii, N. Hiraoka, H. Namatame, and M. Taniguchi, Phys. Rev. B **86**, 115114 (2012).